TECHNISCHE MECHANIK
an open access journal

journal homepage: www.ovgu.de/techmech

Tech. Mech., Vol. 43, Is. 1, (2023), 111–127

Received: 28.01.2023
Accepted: 08.02.2023
Available online: 16.02.2023

Stochastic Modeling of Electrohydrodynamically Enhanced Drag in One-Way and Fully Coupled Turbulent Poiseuille and Couette Flow

Marten Klein[1,2,⋆], Juan A. Medina Méndez[1], Heiko Schmidt[1,2]

[1] Brandenburg University of Technology (BTU) Cottbus-Senftenberg, Chair of Numerical Fluid and Gas Dynamics, Siemens-Halske-Ring 15A, 03046 Cottbus, Germany
[2] Brandenburg University of Technology (BTU) Cottbus-Senftenberg, Energy Innovation Center (EIZ), Scientific Computing Lab (SCL), 03046 Cottbus, Germany

Abstract: Joint predictive modeling of hydrodynamics and electrokinetics is a standing numerical challenge but crucial for various applications in electrochemistry and power engineering. The present lack in modeling of electrohydrodynamic (EHD) turbulent flows lies in the treatment of small-scale processes and scale interactions. To overcome these limitations, a stochastic one-dimensional turbulence (ODT) model is utilized. The model aims to resolve all scales of the flow, but only on a notional line-of-sight, modeling turbulent advection by a stochastically sampled sequence of eddy events that punctuate deterministic molecular diffusive advancement. In this study, two canonical flow configurations are investigated that address different coupling strategies and flow physics. First, EHD effects in a variable-density vertical pipe flow of an ideal gas with an inner concentric electrode are investigated with a one-way coupled model formulation. Electric fields are generated by means of a corona discharge and the corresponding effect of a fixed ionic charge density field. Second, in order to reduce physical complexity, EHD effects the turbulent boundary layers in plane Couette flow of an isothermal univalent ionic liquid are investigated with a fully coupled model formulation. Both application cases demonstrate that ODT has predictive capabilities due to multiscale resolution of transport processes. Present results suggest that more expensive fully than one-way coupling of electrokinetics is crucial when charge relaxation times are significantly larger than the mean advection time scale.

Keywords: drag enhancement, electrohydrodynamic turbulence, high Schmidt number, multiphysical boundary layers, one-dimensional turbulence

1 Introduction

Electrohydrodynamic (EHD) flows are encountered in various technical applications, ranging from power and process engineering, to electrochemistry. Prominent examples are electrostatic precipitation (Robinson, 1968), EHD-enhancement of heat and mass transfer (Laohalertdecha et al., 2007; Bacher and Riebel, 2021), electroconvective flow instability at ion-selective surfaces (Mani and Wang, 2020), turbulent drag control (Ostilla-Mónico and Lee, 2017), hydrogen production in water electrolysis (Shiva Kumar and Himabindu, 2019), and plasma-assisted combustion (Ju and Sun, 2015), among others. The common property among these cases is the vast range of scales that is exhibited by the flow, ranging from large integral lenght scales, down to small molecular viscous and diffusive length scales, as well as EHD length scales, that may fall in the inertial or dissipative range, modifying turbulence scaling properties (Zhao and Wang, 2019). Capturing these scale interactions is a standing numerical challenge that constitutes a lack in modeling and predictability. The present study addresses this lack by a cost-efficient, dimensionally reduced, stochastic modeling approach.

One of the key issues for accurate modeling of wall-bounded EHD flows is the correct representation of transfer processes to and from the wall, as well as capturing of nonlocal and nonlinear interactions between the fluid flow, charge-carrier distributions, and electric fields. These interactions may cause a departure of the turbulence dynamics, e.g., from classical locally homogeneous and isotropic hydrodynamic turbulence (Kolmogorov, 1941) to electrokinetic turbulence (Zhao and Wang, 2017). Indeed, on some EHD regimes, turbulence may appear even at very low Reynolds numbers, e.g., when the electric body forces substitute the role of external inertial forces, and the former are in a large ratio with respect to the viscous forces (Storey, 2005). Direct numerical simulation (DNS) is the preferred method for unraveling the physics of EHD flows. However, DNS is, even to this day, limited by computational cost, which strongly constrains the range of scales that can be resolved. For multiphysics applications, only weakly to moderately turbulent flows can be simulated as expressed by low Reynolds numbers in relation to applications (Duraisamy et al., 2019). Needless to say, ensemble-based parameterizations used in Reynolds-averaged Navier–Stokes simulations (RANS) and diffusive sub-grid-scale closure models used in large-eddy simulations (LES) are of limited applicability in EHD flows, specifically in the presence of walls, due to physical processes that break hydrodynamic universality. A good example in this respect is turbulent drag modification. The physical processes lead to nonuniversal behavior so that, depending on the flow regime and application case, either drag reduction due to flow laminarization or drag increase due to turbulence regeneration may occur (e.g. Nelson et al., 1990; Ostilla-Mónico and Lee, 2017). The mechanisms behind these manifestations of EHD effects have been partly uncovered and can be attributed to some extend to the action of internal spatially varying body forces (e.g. Pandey et al.,

⋆ E-mail address: marten.klein@b-tu.de
doi: 10.24352/UB.OVGU-2023-049

2020) that can be realized by electric fields and charge carriers in EHD flow (e.g. Zhao and Wang, 2021). The present paper aims to contribute to the ongoing discussion by advanced modeling, validation, and prediction by linking drag enhancement effects in a one-way coupled ideal gas flow with those in a fully coupled flow of an ionic liquid.

Alternative to averaged and filter-based turbulence modeling approaches, in this study a fundamentally different, dimensionally reduced, stochastic approach is taken to address modeling issues in EHD turbulence by utilizing the one-dimensional turbulence (ODT) model (Kerstein, 1999). The model formulation and its current capabilities, though not including EHD effects, are also summarized in a recent concept paper on advanced subgrid-scale modeling (Kerstein, 2022). ODT has the capability to capture detailed statistics of complex mixing processes by spatio-temporal resolution of simultaneous scalar and momentum transport processes in the bulk (e.g. Klein et al., 2019), but also in the vicinity of a wall (e.g. Medina Méndez et al., 2019; Klein et al., 2022b). In general, ODT aims to resolve all relevant scales of a turbulent flow but only for a notional line-of-sight represented by a one-dimensional (1-D) domain. A stochastically sampled sequence of mapping events models the effects of turbulent advection by punctuating deterministic processes that are related to molecular diffusion, electric drift currents, Coulomb forces, and boundary conditions. Those processes are directly resolved along the 1-D domain. For the present standalone model application to internal EHD flows, the ODT domain is aligned with the wall-normal coordinate in order to capture transfer processes in the boundary layers. The effects of variable momentum sources, for instance, due to nonhomogeneous electric fields (Medina Méndez et al., 2019), can be resolved if needed but this complication is skipped here. We demonstrate that this modeling strategy captures the leading order physics yielding predictive capabilities for EHD-induced drag enhancement in one-way coupled and fully coupled flow regimes. The predictions of the one-way coupled formulation are validated with available reference experiments, whereas those of the fully coupled formulation are partly validated with available reference direct numerical simulation (DNS) data at low turbulence intensity awaiting experimental validation for moderately and highly turbulent flow.

The rest of this paper is organized as follows. Section 2 gives an overview of the ODT model formulations for multiphysical wall-bounded flows including the extension to one-way coupled and fully coupled EHD flows. In Section 3, we validate the model formulation for a low-Mach number pipe flow of an ideal gas subject to EHD enhancement by comparison to available reference experiments in the one-way coupled flow regime. After that, in Section 4, we apply the fully coupled model to electroconvection of an ionic liquid in plane Couette flow in order to investigate the bulk–boundary layer coupling across flow regimes. We demonstrate that advanced modeling techniques are required in order to address the multiscale nature of wall-bounded the EHD flows. Last, in Section 5, we summarize our findings, give some concluding remarks, and indicate the remaining open issues to be addressed by forthcoming research.

2 Model Formulation

2.1 Overview of the ODT model

In decaying isotropic turbulence seen on a line-of-sight through the turbulent flow (the ODT line), piecewise-transformations on scalar profiles, or triplet maps, induce an increase in the rate of strain, which is characteristic of turbulent eddies. Symbolically, the effect of the triplet map $f(y)$ on an instantaneous profile of the property field $\psi(y)$ is denoted as the transformation $\psi(y) \rightarrow \psi(f(y))$ (in a y-oriented wall-normal domain of a Cartesian coordinate system Kerstein, 1999). The triplet map microscopically models turbulence phenomenology. It takes a property profile along a selected size l interval, compresses the profile to $l/3$, pastes two copies of this profile to fill again, and flips the central copy to ensure continuity.

Such mapping events are stochastically sampled from unknown distribution functions with the aid of a Poisson process (e.g. (Papoulis and Pillai, 2002)). Based on assumed distribution functions for the mapping event size l and location y_0, an efficient thinning-and-rejection method is used for probabilistic selection, in which the local rate (τ^{-1}) of the mappings is calculated in accordance with the local turbulence time scale (eddy turnover time τ). The latter is obtained from the square root of the specific available energy of the current flow state divided by the selected eddy size l. Under absence of body forces, the available energy is governed by the momentary velocity shear across the selected eddy interval (Kerstein, 1999). In the mesh-adaptive model formulation (Lignell et al., 2013, 2018), the specific eddy kinetic energy, l^2/τ^2, is taken proportional to the squared eddy velocity, u_K^2 (Kerstein et al., 2001). This scale velocity is modified when eddy-available potential energy and a scale-dependent viscous penalty energy are taken into account as summarized in Kerstein (2022) and detailed below for the inclusion of EHD effects related to Coulomb forces.

A factor of proportionality that controls the rate of implemented mapping events and , hence, the overall turbulence intensity, is included in the model as a rate parameter, C. The specific eddy-available kinetic energy and the rate-of-strain are related by means of an equivalent turbulent diffusivity. The implementation of a given map at fixed turbulent diffusivity then favors the sampling of further mappings. This is the model representation of the direct energy cascade of three-dimensional (3-D) Navier–Stokes turbulence (Kerstein, 1999). Note that neither the direct cascade nor its scaling exponent is prescribed to the model. The profile modifications resulting from the map applications only represent the turbulence production of sequentially smaller scales by overturning fluid motions in a scale-local fashion not limiting scale interactions.

The set of operations comprising the sampling process and the mappings themselves is known as an eddy event. For decaying isotropic turbulence, there are still two other elements required in the model to complete a consistent dynamic picture of turbulence. One is a mechanism for viscous transport implementation, and the other one is a mechanism for turbulence kinetic energy (TKE) dissipation. Both are a consequence of the viscous momentum flux, which is implemented in a direct way in ODT, by resolving the corresponding numerical fluxes in the 1-D domain after an eddy event has been sampled (Kerstein, 1999). This leads to the formulation of a symbolic 1-D partial differential equation (PDE) for a scalar velocity component ψ in ODT. Specialized to

Cartesian coordinates in a temporal ODT formulation, this is

$$\frac{\partial \psi}{\partial t} + M = -\frac{\partial F(\psi)}{\partial y}. \tag{1}$$

Here, $F(\psi)$ is the model-resolved flux of ψ, e.g., $F(\psi) = -\sigma\,(\partial\psi/\partial y)$ for molecular diffusive gradient fluxes in which σ is a kinematic diffusion coefficient. $M = M(C, \psi, y, f(y))$ represents discrete mapping effects that punctuate deterministic evolution of the conserved scalar $\psi(y,t)$ at discrete times. The mapping effects depend on the selected physical mapping $f(y)$, which models turbulent microstructure, and a turbulent eddy rate parameter C. Note that there is an alternative, so-called spatial ODT formulation, which is generally treated as a reinterpretation of the parabolic temporal ODT formulation. Extensive details on the spatial formulation can be found in other ODT publications (e.g., Lignell et al., 2018; Medina Méndez et al., 2019, 2022).

2.2 Model formulation for temporally developing planar wall-bounded flow

The presence of the confinement wall introduces a dependence on wall-normal location on the turbulent scalar and momentum transport processes. Close to the wall, viscous transport is dominantly one-dimensional, aligned with the wall-normal direction. Away from the wall, viscous transport may have a more inherent 3-D character, although the turbulent transport may dominate instead. The transition between the near-wall and bulk behavior is controlled in ODT in practical terms by the model parameter Z. The latter defines a viscous penalty energy threshold by scaling a viscous damping term below which eddy implementation is effectively suppressed (Kerstein et al., 2001). This imposes the dominance of the viscous transport at the order of the viscous length scale as it primarily affects small scales processes in the vicinity of the wall. However, by construction, viscous suppression may also damp large marginally unstable flow scales since it is an energetic relation that differs from a prescribed mixing length criterion.

Another important dynamical feature in wall-bounded flows is the anisotropy of the velocity statistics. In this context, the role of the turbulent pressure transport is the redistribution of the TKE among the Reynolds stress components (Lee et al., 2016). In ODT, this pressure-scrambling effect is modeled with the aid of a kernel function $K(y) = y - f(y)$ (Kerstein et al., 2001). Eddy events not only implement advective mappings, but also the effects pressure fluctuations that are modeled by the kernel mechanism for the velocity components. Hence, $\psi(y) \rightarrow \psi(f(y))$ for a conserved scalar, and $u_i(y) \rightarrow u_i(f(y)) + c_i K(y)$ for the Cartesian velocity components u_i, $i = 1, 2, 3$. As detailed in Kerstein et al. (2001), c_i is a kernel coefficient calculated based on the available energy and a model parameter $\alpha \in [0, 1]$ that controls the efficiency of inter-component kinetic energy redistribution, such that

$$c_i = \frac{1}{\int_{y_0}^{y_0+l} \rho K^2 \,\mathrm{d}y} \left(u_{i,K} + \mathrm{sgn}\left(u_{i,K}\right) \sqrt{(1-\alpha)\, u_{i,K}^2 + \frac{\alpha}{2}\left(u_{j,K}^2 + u_{k,K}^2\right)} \right). \tag{2}$$

Here, $u_{i,K} = \int_{y_0}^{y_0+l} \rho u_i(f(y)) K(y)\,\mathrm{d}y$, where ρ is the uniform density, and (i, j, k) permutations of $(1, 2, 3)$.

The expression for the local eddy turnover time τ, or, in this case, the local squared eddy rate τ^{-2}, considering $\sum_i u_{i,K}^2$ as the eddy-integrated available kinetic energy for redistribution, as well as the viscous penalty term, which is proportional to the small-scale (viscous) suppression parameter Z, is based on (Kerstein et al., 2001),

$$\tau^{-2} = \frac{2K_0}{\int_{y_0}^{y_0+l} \rho K^2(y)\,\mathrm{d}y} \left(\frac{1}{2} \frac{K_0 \sum_i u_{i,K}^2}{\int_{y_0}^{y_0+l} \rho K^2(y)\,\mathrm{d}y} - \frac{Z}{2} \frac{\mu_{\mathrm{eddy}}^2}{\rho_{\mathrm{eddy}} l^2} \int_{y_0}^{y_0+l} \mathrm{d}y \right). \tag{3}$$

Here, $K_0 = \left(l^2 \int_{y_0}^{y_0+l} \mathrm{d}y \right)^{-1} \int_{y_0}^{y_0+l} K^2(y)\,\mathrm{d}y$, which converges to $4/27$ in the continuum kernel limit. Additionally, μ_{eddy} and ρ_{eddy} are weighted averages of the dynamic viscosity and the mass density within the eddy range $[y_0, y_0 + l]$ (Ashurst and Kerstein, 2005; Lignell et al., 2018). The density and dynamic viscosity of the fluid are assumed as constants, and of uniform value.

Eddy events are sampled in time on the basis of an acceptance probability P_{a}, following a Poisson process. The value of P_{a} for a selected candidate eddy event is calculated as in Kerstein (1999) based on the current flow state. Considering the rate parameter C, the acceptance probability of a selected eddy event given the momentary flow state depends on the location y_0 and size l of the eddy event and is given by

$$P_{\mathrm{a}} = C \frac{\Delta t_{\mathrm{s}}}{\tau} \frac{1}{l^2 \chi(l, y_0)} < 1. \tag{4}$$

Here, Δt_{s} is a sampling time interval that needs to be able to resolve any possible eddy turnover time τ. Hence, we select $\Delta t_{\mathrm{s}} < \tau$, which is adapted dynamically in the implementation (see Kerstein et al., 2001). Furthermore, $\chi(l, y_0)$ is a guessed joint probability density function (p.d.f.) of eddy event sizes and locations which is used to obtain reasonable candidate events by assuming turbulent cascade phenomenology. Oversampling and rejection guarantees that ODT simulation results are insensitive to the exact choice of this joint p.d.f. as long as the region of nonzero probability density extends over the entire range of physically relevant eddy sizes and locations.

After an eddy event is implemented, the deterministic evolution is comparable to that in Eq. (1). With the model-resolved deterministic molecular viscous flux $F_i(u_i) = -\nu\,(\partial u_i/\partial y)$, the stochastic operators M_i and K_i representing the map-induced

changes and kernel effects due to turbulent eddies, surplus external momentum sources S_i, we obtain profile evolution equations for the three velocity vector components $u_i(y,t)$, $i = 1, 2, 3$, as

$$\frac{\partial u_i}{\partial t} + M_i + K_i = S_i + \nu \frac{\partial^2 u_i}{\partial y^2}. \tag{5}$$

This expression incorporates now symbolically the effects of the kernel, and of the energy redistribution among velocity components, by means of the term $K_i(C, Z, \alpha, u, f(y))$. S_i is a source term for the i-th velocity component to be integrated together with the viscous flux, for example, a fixed pressure gradient (FPG) or another, possibly variable, body force.

2.3 Extension to spatially developing flow with variable density effects

The model formulation presented in Section 2.2 considers the temporal change of scalar profiles along a line-of-sight through the turbulent flow, and is generally referenced as T-ODT. An extension of the model to capture streamwise fluxes of spatially evolving flows (e.g., boundary-layer-type flows) has been presented in Kerstein (1999) and Ashurst and Kerstein (2005), and is denoted by S-ODT. More importantly, Ashurst and Kerstein (2005) also present a variable-density formulation for low Mach number flows. In both variable-density T-ODT and S-ODT, a second kernel function $J(y) = |K(y)|$ is introduced in order to facilitate enforcement of physical conservation principles.

For variable-density flow, the various integral expressions above receive the mapped mass density such that $\rho \longrightarrow \rho\big(f(y)\big)$. In variable density T-ODT, the calculation of the available kinetic energy $u_{i,K}$ changes accordingly. The fractions $u_{i,K} \Big/ \int_{y_0}^{y_0+l} \rho K^2(y)\,\mathrm{d}y$ and $u_{i,K}^2 \Big/ \left(2\int_{y_0}^{y_0+l} \rho K^2(y)\,\mathrm{d}y\right)$ in Eqs. (2) and (3), change to $P_i/(2S)$ or $P_i^2/(4S)$, respectively, where (Ashurst and Kerstein, 2005)

$$P_i = u_{i,K} - H \int_{y_0}^{y_0+l} [\rho u_i]\big(f(y)\big)\, J(y)\,\mathrm{d}y, \tag{6}$$

$$S = \frac{H^2+1}{2} \int_{y_0}^{y_0+l} \rho\big(f(y)\big)\, K^2(y)\,\mathrm{d}y - H \int_{y_0}^{y_0+l} \rho\big(f(y)\big)\, J(y)\, K(y)\,\mathrm{d}y, \tag{7}$$

$$H = \frac{\int_{y_0}^{y_0+l} \rho\big(f(y)\big)\, K(y)\,\mathrm{d}y}{\int_{y_0}^{y_0+l} \rho\big(f(y)\big)\, J(y)\,\mathrm{d}y}, \tag{8}$$

where P_i, H, and S (to be distinguished from the momentum sources S_i) are kernel coefficients used to generalize c_i in Eq. (2). In the S-ODT model, the streamwise change of the scalar profiles in the line-of-sight through turbulence is studied. Two variants arise in this case. One is the conservative boundary-layer formulation (Ashurst and Kerstein, 2005), and another the non-conservative wall-constrained internal-flow formulation (Medina Méndez et al., 2019). Essentially, in S-ODT, all integrals in Eqs. (6)–(8), as well as the integrand of $\int_{y_0}^{y_0+l} \rho K^2(y)\,\mathrm{d}y$ in the prefactor in Eq. (3), receive an additional multiplication by $u(f(y))$, the mapped streamwise advecting velocity (for details see Medina Méndez et al., 2019; Ashurst and Kerstein, 2005). The time scale τ changes to a streamwise length scale ξ, and the temporal sampling Δt_s changes to a streamwise sampling Δx_s (Ashurst and Kerstein, 2005). Symbolically, the S-ODT equivalent of Eq. (5) has a modified left-hand side and reads

$$u\frac{\partial u_i}{\partial x} + M_i + K_i = S_i + \nu \frac{\partial^2 u_i}{\partial y^2}. \tag{9}$$

2.4 Extensions to cylindrical geometry

An additional model extension, or a generalization of the T-ODT and S-ODT formulations for both planar and cylindrical flows, considering a dynamically adaptive mesh, was presented in Lignell et al. (2018). The cylindrical formulation replaces the planar coordinate y for the radial coordinate r, while any line-integral $\int(\cdot)\,\mathrm{d}y$ in all of the equations presented so far, changes to a surface radial integral of the form $\int(\cdot)\, r\,\mathrm{d}r$. Eqs. (1) and (9) also consider a change in the form of the gradient flux. The generalized scalar conservation equation, Eq. (1), becomes

$$\frac{\partial \psi}{\partial t} + M(\psi, C, Z, r, f(r)) = -\frac{1}{r}\frac{\partial\,(rF(\psi))}{\partial r}, \tag{10}$$

where $F(\psi) = -\sigma\,(\partial\psi/\partial r)$ for the model resolved radial molecular diffusive flux. The specific form of the viscous flux for every velocity component in the cylindrical coordinate system is given in Medina Méndez et al. (2019).

Note that Medina Méndez et al. (2019) also introduce a variable-density formulation in which the density is treated as an active scalar, coupled with the evolution of the temperature. The temperature and density states are coupled by the ideal gas law and the divergence condition during the deterministic evolution between subsequent eddy events. This procedure is the equivalent of the enforcement of mass and energy conservation.

2.5 Incorporation of EHD effects

The main goal of this study is the capturing of leading-order EHD effects in internal flows that are associated with a modification of the boundary-layer dynamics. Hence, the ODT-based 'minimal flow model' shall be able to capture wall-normal contributions to nonuniversal EHD turbulence circumventing computation of 3-D electric fields. For the standalone ODT application to EHD pipe and Couette flows considered here, it is assumed that all property fields are not only statistically but also momentarily approximately homogeneous in the lateral directions. Available reference DNS (Ostilla-Mónico and Lee, 2017) indicate that this assumption is reasonable at least for weakly turbulent boundary layers with relatively large charge relaxation time scales.

It is well known that EHD effects modify turbulence properties (e.g. Zhao and Wang, 2019) which suggests to incorporate them in the eddy rate expression by an additional eddy-integrated energy term that enters the bracket in Eq. (3). The formulation of an electrostatic potential energy term is based on a mathematical analogy of electrostatic potential energy to gravitational potential energy. In the latter, mass density variations affect the flow if it experiences a background gravity field (Kerstein, 1999; Wunsch and Kerstein, 2005). Hence, electric charges take the role of mass inhomogenieties and the electric field the role of the gravitational acceleration. The starting point is the buoyancy treatment within the ODT vector velocity formulation described in Gonzalez-Juez et al. (2013) and, with some more generalization, in Kerstein (2022).

ODT modeling of EHD effects requires the implementation of an appropriate form of the Coulomb forces and an account of the change in electrostatic potential energy within in the ODT eddy sampling procedure. The Coulomb force density is given by $\rho_\mathrm{f} E_i$, where $\rho_\mathrm{f} = e(n_+ c_+ - n_- c_-)$ is the continuum density of free charges due to positively (+) and negatively (−) charged scalars (i.e., electrochemical species or tracers) with concentration $c_\pm$ and valence $n_\pm$ multiplying the unit charge e on an electron, and by Faraday's law for nonmagnetic media, the electric field $E_i = -\partial\Phi/\partial x_i$, where Φ denotes the total electrostatic potential and $(x_i) = (x, y, z)^\mathrm{T}$ the Cartesian coordinates. The concentrations $c_\pm$ obey individual scalar conservation equations similar to Eq. (1), but also other formulations specializing to electron an ion currents are possible. On the one hand, Coulomb forces acting perpendicular to the ODT domain can be included straightforwardly as source term S_i in the ODT momentum equation, Eq. (5), driving turbulence by an increase of velocity shear (Medina Méndez et al., 2019). On the other hand, Coulomb forces acting along the ODT domain affect the eddy rate expression, Eq. (3). Under presence of electric fields and free electric charges, redistribution of fluid parcels by mapping results in an additional eddy-integrated electrostatic potential energy term that physically modifies the eddy sampling rate in analogy to gravitational potential energy (Kerstein, 1999; Wunsch and Kerstein, 2005).

The form of the change in electrostatic potential energy, ΔE_pot, results from the work performed on the fluid due to the energy release from the pre-mapped to the post-mapped state analogous to buoyancy within the velocity vector model formulation of Gonzalez-Juez et al. (2013) and its generalization presented in Kerstein (2022). ΔE_pot has to be added within the square bracket of Eq. (3) for EHD-enhanced sampling. Likewise, it requires a multiplication by $4S$ under the square root of Eq. (2) for potential energy redistribution due to the mapping kernel $K(y)$ in the notation of Lignell et al. (2013, 2018). The following eddy-integrated electrostatic potential energy has to be inserted in the bracket in Eq. (3),

$$\Delta E_\mathrm{pot} = -\int_{y_0}^{y_0+l} \Big[\rho_\mathrm{f}(f(y))\,\Phi\big(\rho_\mathrm{f}(f(y))\big) - \rho_\mathrm{f}(y)\,\Phi\big(\rho_\mathrm{f}(y)\big)\Big]\,\mathrm{d}y. \tag{11}$$

In addition to this equation and the solution of Eq. (5), the 1-D conservation equation for ρ_f, and the Nernst–Planck equation, are solved together with the 1-D representation of Gauss' law for the electric potential, $\partial(\varepsilon E_i)/\partial x_i = \rho_\mathrm{f}$, as well as Faraday's law, $E_i = -\partial\Phi/\partial x_i$, for a known electric permittivity ε and the dynamically resolved component E_2, which is acting along the ODT domain and, hence, energetically influences the turbulent eddy implementations.

Note that the transfer of electrostatic potential energy to kinetic energy of the flow, or *vice versa*, is the mechanism for implementation of the effects of the work performed by the flow against Coulomb forces by a notional eddy turnover, represented as the instantaneous application of the triplet map $f(y)$ for the wall-normal coordinate y. For the application cases analyzed here, only the effects of a resolved electric field along the ODT line are considered, thus any electrostatic potential energy involved in the formulation is due to the resolved E_2 component of the electric field. Non-resolved components E_1 and E_3, that are zero on average for the cases at hand, are neglected. In that sense, there is no *direct* contribution to the mean kinetic energy by $\rho_\mathrm{f} E_i$, given that the modeled effect is simply seen as a modification of the pressure gradient in the line direction. Any EHD-enhancement (or loss), is then a consequence of a modified fluctuating pressure transport, which is modeled in ODT by the kernel kinetic energy redistribution. This is the formulation equivalent of a modification in the Reynolds stress tensor components, which is conceptually comparable to the discussion in Davidson and Shaughnessy (1986) on the effect of electric body forces.

To summarize the model extension to EHD turbulence, overturning fluid motions modeled by ODT mapping events may lead to gain or loss of kinetic energy, which makes such fluid motions more or less plausible. The work is done against the electric forces by relocation of free electric charge carriers in the background electric field, surplus modification of the background field which implies a change in the electrostatic potential energy associated with the configuration of charges in the current flow state. Inclusion of the former effect is denoted as one-way coupling, whereas inclusion of both effects is denoted as fully coupling, respectively. In the one-way coupling case, the Nernst–Planck equation reduces to a zero-divergence condition for the electric current density (Melcher, 1981; Medina Méndez et al., 2022). This results then in a constant and uniform electric (drift) current density along the ODT line for the planar Cartesian case. Electroquasistatic fields are calculated before hand and remain fixed during the simulation. Despite the constancy of the fields, the transfer of electrostatic potential to kinetic energy still takes place, specifically in the momentum direction aligned with the ODT line. Given that the velocity component in the direction of the ODT line is merely an energy container for the purpose of the ODT kernel mechanism within the ODT velocity vector formulation (Kerstein et al., 2001), the transfer of energy represented by the change in Eq. (11) must be nonzero. Thus, ρ_f is allowed to fluctuate due to the effect of turbulent advection (triplet maps), irrespective of the constancy of Φ, which is due to the prescribed

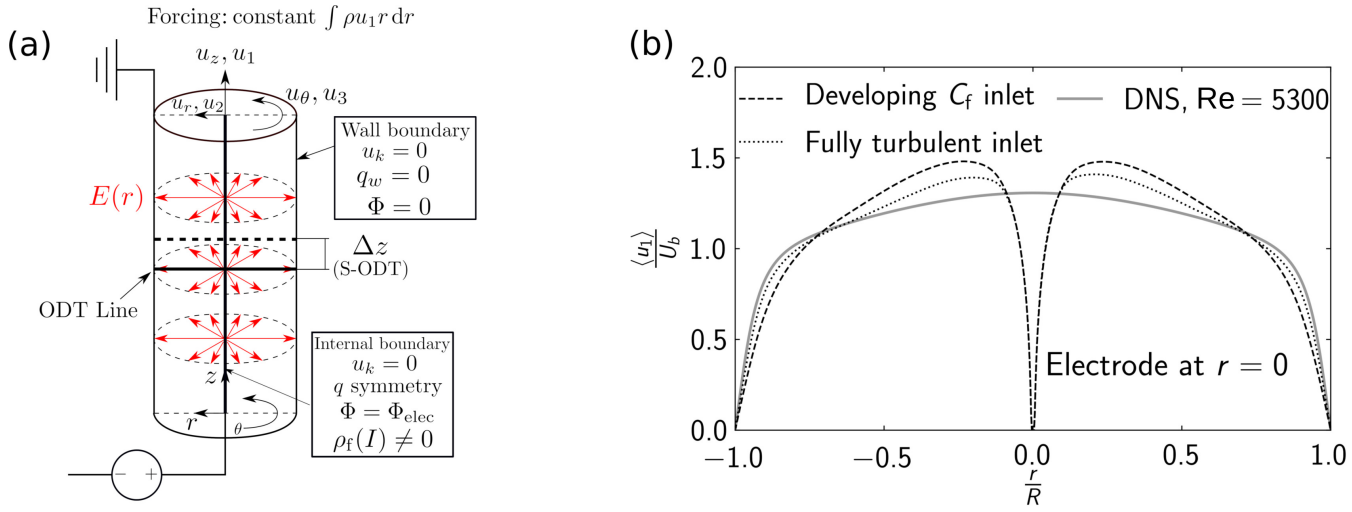

Fig. 1: (a) Sketch of the spatially developing (S-ODT) simulation for EHD-enhanced vertical pipe flow. $\rho_f(I) \neq 0$ refers to the nonzero Dirichlet boundary condition value for the free electric charge density at the electrode, which is parameterized as a function of the supplied electrical current I assuming presence of a corona discharge. (b) Averaged streamwise velocity profiles for the incoming flow evaluated in ODT. Reference DNS from Khoury et al. (2013) for fully developed streamwise homogeneous circular pipe flow with Re = 5300 are given for comparison. Reference DNS exhibits a slightly larger Re than present ODT simulations as seen by smaller velocity gradients at the wall in ODT.

equilibrium background state in the one-way coupled regime, causing a corresponding change in ΔE_{pot}. For fully coupling, the Nernst–Planck equations maintain a form similar to Eq. (1). An explicit numerical solver is used in which the model resolved instantaneous profile of the electrostatic potential, e.g., $\Phi(y)$ in the planar Cartesian case, is obtained by numerical solution of a 1-D Poisson equation by application of the Thomas algorithm whenever $\rho_f(y)$ has changed.

3 Drag Enhancement in One-Way Coupled EHD Vertical Pipe Flow

We now discuss some issues encountered in the simulation of one-way coupled EHD-enhanced pipe flows. These type of flows resemble the practical application of industrial electrostatic precipitators (ESPs). Reference experimental work on cylindrical wire-tube ESPs was carried out by Nelson et al. (1990), and is considered here as a reference study for the purpose of comparison of the EHD-enhanced drag. The discussion presented here complements the study published in Medina Méndez et al. (2022), where the reader can find extensive details concerning the overview of the model, simulation input parameters, and the analysis concerning EHD effects on drag. The interested reader is encouraged to review Medina Méndez (2020) for the full model derivation, rationale, and previous canonical flow validations leading to the EHD-enhanced case.

3.1 Flow configuration and model set-up

Fig. 1(a) shows the simulation set-up for the EHD pipe flow. The set-up consists of a cylindrical tube of radius $R = 1.6 \times 10^{-2}$ m. There is an electrode concentric with the tube, of radius $R_{\text{elec}} = 1.25 \times 10^{-4}$ m and length $B_{\text{elec}} = 2.05$ m, which is the reason why this type of devices is usually known as a wire-tube ESP (e.g. Bacher et al., 2020). The experimental device has a test section length $B_{\text{TS}} = 1.02$ m, which is where actual measurements take place. The entry section length of the experimental device, which aims to remove flow developing effects on the measurements, has a length $B_{\text{entry}} = 1.59$ m. These specifications correspond to the reference experiment by Nelson et al. (1990). The inlet gas flow is at atmospheric pressure and assumed as air, taken as an ideal gas with molecular Prandtl number $\text{Pr}_{\text{air}} \simeq 0.71$ and uniform fluid properties defined at the reference temperature $T_0 = 300.15$ K. We evaluate flow conditions based on the prescribed bulk velocity $U_b = 2\,\text{m}\,\text{s}^{-1}$, yielding the associated bulk Reynolds number $\text{Re} = 2RU_b/\nu = 4000$, based on the tube diameter $2R$.

In order to compare flow statistics with the reference experimental data from Nelson et al. (1990), some issues concerning the device geometry must be addressed. The presence of the entry section length, plus the issue of an electrode with a length which does not coincide with the test section length, are neglected in the flow configuration shown in Fig. 1(a). To that extent, the length of the device is taken equal to the nominal test section (TS) length, B_{TS}. This causes an issue with the reported voltage–current values of the experiments in Nelson et al. (1990) (voltage–current characteristic curves). Indeed, the electro-quasistatic divergence condition for the electrical (drift) current density J, demands that $J(r) \sim r^{-1}$, hence the radially weigthed current density is constant, $Jr = \text{const}$ (Melcher, 1981; Medina Méndez et al., 2022). Additionally, consider that I, the electrical current on the electrode, can also be defined as the integral of J over a given surface S enclosing the central wire electrode. Due to the reduced dimensional character of our analysis, and the absence of further information in Nelson et al. (1990), we assume that I is uniform throughout any test section surface defined as $S_r = 2\pi r B$, for any value $R_{\text{elec}} \leqslant r \leqslant R$ and a given axial length B. Then, there is clearly a change in $I = JS_r$, depending on whether S_r is defined with $B = B_{\text{TS}}$ or $B = B_{\text{elec}}$. Since the dimensionless equivalent of I must be the same in experiments and simulations, we recalculate the current from the reported experimental current values I_{exp}

Tab. 1: Voltage-current characteristic values used in the numerical simulations.

Voltage $\Phi = \Phi_{\text{elec}}$, (V)	Electric current, I (A)	Masuda number Md	EHD number N_{EHD}
0	0	0	0
6500	$\approx 7.2 \times 10^{-5}$	$\approx 2.0 \times 10^{4}$	≈ 116
7000	$\approx 4.0 \times 10^{-4}$	$\approx 1.3 \times 10^{5}$	≈ 334
7750	$\approx 1.2 \times 10^{-3}$	$\approx 3.2 \times 10^{5}$	≈ 563

following Nelson et al. (1990) (measured for B_{elec}), but apply the geometrical correction factor $B_{\text{elec}}/B_{\text{TS}}$. This yields the correct electrical current density J (and, thus, the radius-weighted quantity Jr) to use for the simulations (Medina Méndez et al., 2022). Tab. 1 shows the utilized voltage–current characteristic values for the numerical simulations. Note that the electrode discharge is positive, thus, only simulations corresponding to a positive corona discharge are evaluated. Tab. 1 shows two dimensionless parameters associated to the voltage–current values: Md is the Masuda number, which characterizes the voltage, and is defined as $\text{Md} = \varepsilon_0 \, \Phi_{\text{elec}} \, (\Phi_{\text{elec}} - \Phi_{\text{on}}) \, / \, (\rho_0 \nu_0^2)$, where ε_0 is the vacuum electrical permittivity, Φ_{elec} is the operating voltage at the discharge electrode, which is represented at the internal boundary in Fig. 1(a), Φ_{on} is the onset voltage for electrical discharge in air, and ρ_0 and ν_0 are reference values for the density and kinematic viscosity. Also, N_{EHD} is the EHD number, characterizing the electric current I, defined as $N_{\text{EHD}} = \sqrt{(IR^3\rho_0)/(S_R \beta_{\text{f}} \mu_0)}$, where S_R is S_r evaluated for $r = R$ and $B = B_{\text{TS}}$, $\mu_0 = \rho_0 \nu_0$, and β_{f} is a uniform and constant ionic mobility for positive corona discharge.

Another important issue which was only deduced in retrospect to the analysis put forward by Medina Méndez et al. (2022), is that the inflow condition plays a major role in the observed drag enhancement. This is a finite Reynolds number effect, sensible due to the relatively low Re = 4000 used here. For further elaboration, we consider the hydrodynamic length estimation from Abraham et al. (2008),

$$L_{\text{FD}} = 2R \left(2.4 \times 10^{4} \, \text{Re}^{-0.68} \right). \tag{12}$$

For Re = 4000, the above formula yields the length scale $L_{\text{FD}} = 2.7287$ m after which the flow would be fully developed (FD). L_{FD} is larger than B_{entry}. In fact, $L_{\text{FD}} > B_{\text{entry}} + B_{\text{TS}}$. As standalone 1-D tool that utilizes a map-based representation of 3-D turbulence for representative 1-D flow profiles, ODT can not capture all features of developing Navier–Stokes flows. Therefore, it is not possible to run a simulation for developing flow and confidently evaluate the statistics of the flow. Nevertheless, it possible to verify the effects of the developing flow on global quantities, such as the friction factor C_{f}, based on the model-resolved flow physics. Hence, we evaluate two inlet conditions in our simulations: the first one is for a fully developed turbulent inlet flow at Re = 4000, and the second one is for an inlet flow which has an equivalent developing flow friction factor $C_{\text{f}}(B_{\text{TS}} + B_{\text{entry}})$. The former developing C_{f} is calculated by the formula shown in Abraham et al. (2008) for developing flow, using the suggested developing flow pressure drop factor curve, and the length $L = B_{\text{TS}} + B_{\text{entry}}$. Average streamwise velocity profiles for the two types of inlet flow conditions are shown in Fig. 1(b), along with reference pipe flow DNS data for a slightly larger Reynolds number (Khoury et al., 2013). It is noted that we use an average procedure denoted by the operator $\langle \cdot \rangle$, which is an ensemble of realizations. In the case of Fig. 1(b), the inlet flow profiles shown correspond to an ensemble average of stochastic turbulent inlet conditions, which were generated using T-ODT simulations of constant property flow. Specifically, T-ODT simulations used model parameters $C = 3$, $Z = 350$ and $\alpha = 2/3$ to generate the fully developed inlet turbulent flow profiles. The C parameter was then adjusted in order to generate the equivalent developing C_{f} flow profiles, given that a variation in C can be used to change the slope of the mean velocity profile in the outer layer (Fragner and Schmidt, 2017; Rakhi et al., 2019), thus modifying the obtained value of C_{f}.

As discussed previously, during the simulations, we only consider one-way coupled electric fields, with the implications suggested in Sec. 2.5. Electric charges (positive ions in air) are assumed as a continuum phase, such that a charge density field ρ_{f} can be represented in ODT. Besides the inlet flow conditions, the simulations also observe a set of two boundary conditions. The wall boundary conditions are applied at $r = R$, and consist of the no-slip condition for the velocity components, an adiabatic flow condition, i.e., a zero wall heat-flux $q_{\text{w}} = \sigma(\partial T/\partial r)|_{\text{w}} = 0$, where T is the temperature and σ is the thermal conductivity, and a zero voltage for the ESP collector wall (subscript w). The electrode boundary conditions consist of an internal boundary in which the following conditions are applied: no-slip for the velocity components, symmetry imposition for the heat flux q, the operating voltage Φ_{elec} for the electrostatic potential, and an implicit value for the charge density ρ_{f}, which is obtained from the supplied ESP current I. The internal boundary condition for the velocity profile can be seen clearly in Fig. 1(b), which contrasts with profiles obtained from a traditional pipe flow simulation. For details on the generation of the constant electro-quasistatic (EQS) fields, please refer to Medina Méndez et al. (2022); Medina Méndez (2020). Note also that the temperature is solved together with the velocity in the ODT simulations. Joule heating is incorporated as a source term in the temperature equation, which is also detailed in Medina Méndez et al. (2022) and Medina Méndez (2020). Finally, and as shown in Fig. 1(a), we recall the assumption of statistically homogeneous azimuthal flow, as well as the enforcement of a constant streamwise mass flux in the ODT simulations.

3.2 Darcy friction factor and skin friction coefficient

This section focuses on the evaluation of the friction drag, and its relation with the average streamwise pressure gradient of the flow. S-ODT simulation results presented here were obtained using the model parameters $C = 2$, $Z = 100$ and $\alpha = 2/3$. In a statistically stationary and statistically streamwise homogeneous pipe flow, the axial wall pressure gradient is related to the wall shear stress by

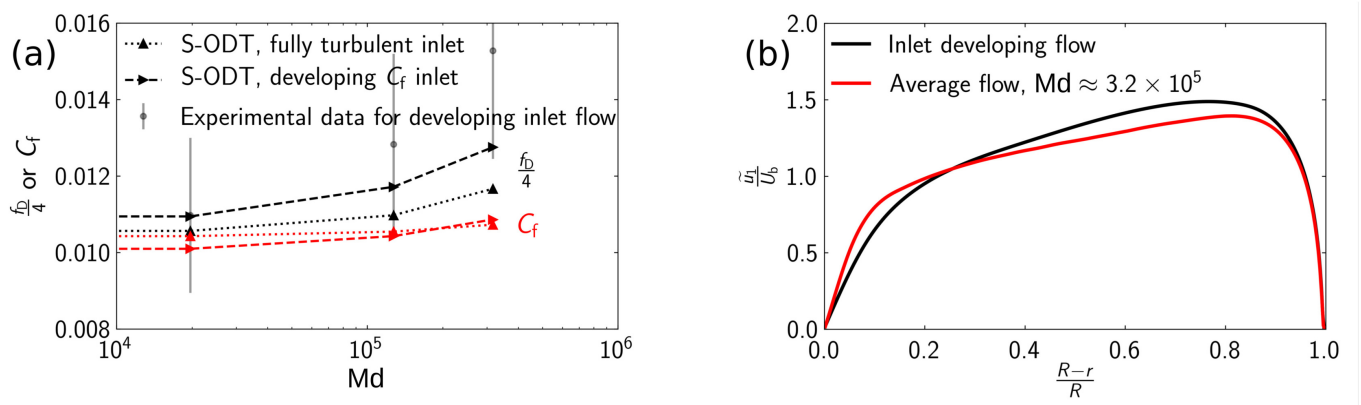

Fig. 2: (a) ODT prediction of the enhancement of the Darcy friction factor f_D (black) and the skin friction coefficient C_f (red) with the dimensionless EHD body force expressed as Masuda number Md. Reference experiments are from Nelson et al. (1990). (b) Simulated radial profiles of the mean axial velocity for the inflow condition without EHD effects (black) and the developed flow with EHD effects (red) across the pipe radius. The outer wall is located on the left and the electrode at the right. The friction factor enhancement is a result of increased turbulent mixing as indicated by an increase of the velocity gradient at $r = R$ and a flatter bulk profile.

the known relation

$$\left(\frac{\mathrm{d}\bar{p}_\mathrm{w}}{\mathrm{d}z}\right)_{\text{pipe flow}} = -\frac{2\tau_\mathrm{w}}{R}. \tag{13}$$

Here, $\bar{p}_\mathrm{w} = \bar{p}$ is the wall pressure, which is equivalent to a uniform pressure in the radial direction for low Mach number flows. Likewise, τ_w is the wall shear stress. In contrast to Eq. (13), the EHD-enhanced pipe flow simulations following the set-up shown in Fig. 1(a) involve a significantly more complex axial pressure gradient. First of all, $\bar{p}$ is no longer uniform in the radial direction, given the appearance of a radial pressure gradient due to the presence of the Coulomb or EHD body force (Robinson, 1968). Following Medina Méndez et al. (2022), the wall pressure difference between the inlet and the outlet of the ESP is given by

$$\Delta p_\mathrm{w} = -\frac{2}{R^2}\,\Delta\left(\int_0^R \langle\rho u_1 u_1\rangle\, r\,\mathrm{d}r - R^2\left(\langle\mu\rangle\frac{\partial\langle u_2\rangle}{\partial r}\right)\bigg|_R\right) - \frac{2}{R^2}\,\Delta\left(\int_0^R \langle\mu\rangle\frac{\partial\langle u_2\rangle}{\partial r}\, r\,\mathrm{d}r\right) - \frac{2}{R}\int_0^{B_\mathrm{TS}} \tau_\mathrm{w}\,\mathrm{d}z - \frac{Jr}{\beta_\mathrm{f}}, \tag{14}$$

where Δ refers to a difference between the location of the outlet ($z_\mathrm{out} = B_\mathrm{TS}$) and the inlet (e.g., $z_\mathrm{in} = 0$) of the simulated device. We remind that, here, $Jr = I/(2\pi B_\mathrm{TS})$ is constant and uniform, calculated with the help of I from the (corrected) voltage–current curves in Nelson et al. (1990), or from the values in Tab. 1. We stress again the use of the ensemble average operator, using a given number of ensemble members N_ens, to obtain the averaged quantities required for Eq. (14). We have used $N_\mathrm{ens} = 60$ for the results presented here. The calculation of Δp_w allows an approximation of $\mathrm{d}\bar{p}/\mathrm{d}z$ as $\Delta p_\mathrm{w}/B_\mathrm{TS}$. Since f_D is calculated by a $\mathrm{d}\bar{p}/\mathrm{d}z$ which is not related to the wall shear stress as in Eq. (13), Nelson et al. (1990) present the Darcy friction factor as a way to represent the dimensionless pressure gradient,

$$f_D = -\frac{4R}{\rho_\mathrm{b} U_\mathrm{b}^2}\frac{\mathrm{d}\bar{p}}{\mathrm{d}z}. \tag{15}$$

For reference, we also calculate directly the wall shear stress and the associated skin friction coefficient C_f, which is simply given by the traditional definition involving the ratio between the wall shear stress and $\rho_b U_b^2/2$, the product of the bulk density and the specific bulk kinetic energy (Pope, 2000). For the purpose of comparing with the integral global quantity f_D, we use a streamwise averaged $\tilde{\tau}_\mathrm{w}$ for the calculation of C_f, such that

$$\tilde{\tau}_\mathrm{w} = \frac{1}{B_\mathrm{TS}}\int_0^{B_\mathrm{TS}} \tau_\mathrm{w}\,\mathrm{d}z = \frac{1}{B_\mathrm{TS}}\int_0^{B_\mathrm{TS}} \left(\langle\mu\rangle\frac{\partial\langle u_1\rangle}{\partial r}\right)_{r=R} \mathrm{d}z \tag{16}$$

It is noted that $f_D = 4C_f$ for standard pipe flows, yet the identity is not maintained for the EHD-enhanced flows presented here. In this context, there is no available reference data for the comparison of C_f. Fig. 2(a) shows the results for the evaluation of f_D, presented as $f_D/4$. The value of C_f is also presented in Fig. 2(a). Furthermore, averaged velocity profiles for the developing inlet flow case are presented in Fig. 2(b) for completion in the assessment of the EHD-enhanced drag. Both the average inlet flow conditions and the streamwise and ensemble averaged streamwise velocity $\tilde{u}_1$ for the largest Md case are compared to each other.

3.3 Discussion

Fig. 2(a) shows that for the case of the developing flow inlet, there is a difference, even at zero EHD body force, between $f_D/4$ and C_f, which is precisely the effect caused mainly by the axial gradient of average kinetic energy in Eq. (14). At larger Md, the

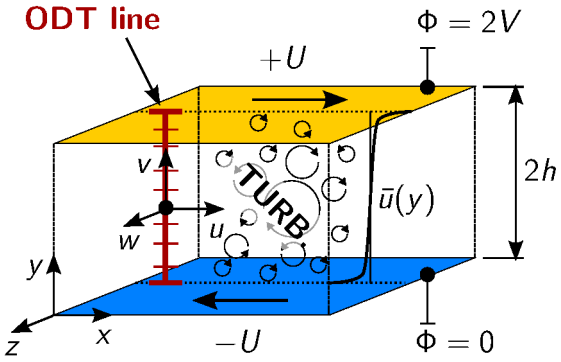

Fig. 3: Sketch of the EHD Couette configuration with temporally developing flow. The one-dimensional domain (ODT line) is fixed in space and approximately taken as closed system in order to facilitate utilization of ODT as standalone model.

difference between $f_D/4$ and C_f increases due to the appearance of ever larger values of the Coulomb force or EHD body force in Eq. (14). The increase in the difference with respect to Md is maintained for the fully developed turbulent inlet flow simulated case, however, the magnitude of the difference is reduced in comparison to the developing flow inlet. The assessment of the drag enhancement due to EHD is facilitated by the observations obtained from Fig. 2(b), where we note both the decrease of the profile in the outer layer of the flow, and the increase of the near wall gradient. As a final comment, we note that, despite the variable temperature and density effects being simulated in S-ODT, variations in the temperature and fluid properties remained almost negligible in the evaluated case, with only a local temperature increase very close to the electrode.
ODT is a reduced order model. In this part of the study, we have shown that, even though the friction factor evaluation is simply an integral quantity of the flow, the results obtained by the ODT simulations are worth commenting due to the multiphysical nature of the application. This is neither an application that can be easily evaluated by DNS nor treated faithfully with LES or RANS. ODT provides small-scale resolution and dynamical complexity by capturing relevant physical processes at feasible cost. The relative contributions to the pressure gradient according to Eq. (14) are thus model predictions. It has been verified that the largest contribution to $\mathrm{d}\bar{p}/\mathrm{d}z$ is due to the wall shear stress τ_w, and in second place, by the average kinetic energy gradient. The latter is the reason why the utilization of developing flow inlet conditions are necessary to obtain a model prediction that reasonably captures the reference experiments.

4 Drag Enhancement in Fully Coupled EHD Couette Flow

In this section, we consider a simple model for strongly coupled wall-bounded shear-driven EHD turbulence in an ionic liquid utilizing a planar Couette configuration.

4.1 Flow configuration and model set-up

Fig. 3 shows a sketch of a simple electroconvection configuration based on plane Couette flow. The set-up corresponds with the reference DNS by Ostilla-Mónico and Lee (2017). The top wall is moving and held at a different voltage relative to the bottom one. No-slip isopotential zero-flux wall-boundary conditions are prescribed. The T-ODT model set-up uses $C = 10$, $Z = 600$, $\alpha = 2/3$ as calibrated for low-Reynolds-number hydrodynamic channel flow (Lignell et al., 2013) and used for the preliminary EHD studies by Klein and Schmidt (2020, 2021). The EHD-enhanced flow reaches a statistically stationary state like the canonical case without EHD effects so that the continuous and conditional statistical analysis follows Kerstein (1999) and Klein et al. (2022b) for the momentum and scalar transport, respectively. The ionic liquids considered are univalent electrolytes with neutral bulk charge, consisting of two identical ionic scalar species $\psi = c_\pm$ with the same valence and mobility but opposite charge, dissolved in a dielectric fluid (e.g., water). The model-resolved deterministic ion fluxes in accordance with Eq. (1) thus have diffusive and drift contributions, yielding

$$F_\pm(c_\pm) = -D\frac{\partial c_\pm}{\partial y} \mp \frac{Dc_\pm}{V_T}\frac{\partial \Phi}{\partial y}. \tag{17}$$

In analogy to Ostilla-Mónico and Lee (2017), scaling of the Poisson–Nernst–Planck and Navier–Stokes equations (or the dimensionally reduced ODT representation of them) yields five dimensionless control parameters that define the flow state: the bulk Reynolds number, $\mathrm{Re} = Uh/\nu$, the ionic Schmidt number, $\mathrm{Sc} = \nu/D$, the fixed dimensionless voltage, $\hat{V} = 2V/V_T = 10$, the fixed coupling constant, $\beta = \varepsilon V_T^2/(\rho\nu D) = 0.5$, and the fixed normalized Debye layer thickness, $\lambda_D/h = \sqrt{\varepsilon V_T/(2\rho c_0 e h^2)} = 0.01$, unless mentioned otherwise. In these expressions, U denotes the prescribed wall velocity magnitude, h the channel half-height, $V_T = k_B T/e$ the thermal voltage, in which k_B denotes the Boltzmann constant and T the approximately uniform ambient temperature, D the kinematic diffusivity of the ions in the electrolyte, and c_0 the uniform initial concentration of the univalent ion species, respectively, in addition to the other physical parameters introduced above.
Note that Re is the only direct control parameter for the flow regime. $\hat{V}$ is an additional control parameter that parameterizes the internal energy and thus takes the role of an equation of state. The three remaining parameters are related to the electrolyte: Sc gives the ratio of the viscous and scalar (ionic) diffusion coefficients; λ_D/h is a relative measure of electric charge separation that

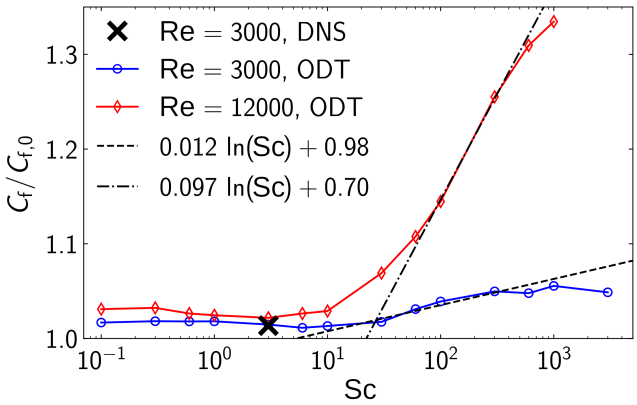

Fig. 4: ODT prediction of the turbulent drag enhancement as function of Sc for low and moderate Re keeping $\hat{V} = 10$, $\beta = 0.5$, $\lambda_D/h = 0.01$, and adjustable model parameters fixed. ODT predicts a logarithmic increase of the skin friction coefficient with Sc for nonsaturated drag enhancement, given by $C_f/C_{f,0} = A' \ln(\mathrm{Sc}) + B'$ for $\mathrm{Sc} \in [50, 500]$. Here, the fit coefficients A' and B' only retain a dependence on Re. Reference DNS (×) data is from Ostilla-Mónico and Lee (2017).

Tab. 2: Skin friction coefficient $C_{f,0}$ for Couette flow without EHD effects ($\hat{V} = 0$) comparing ODT results with published data.

Re	$C_{f,0}$	Reference
3000	$\approx 6.5 \times 10^{-3}$	DNS (Pirozzoli et al., 2014)
3000	$\approx 6.0 \times 10^{-3}$	experiments (Robertson, 1959)
3000	$(5.9 \pm 0.4) \times 10^{-3}$	present ODT
12,000	$\approx 4.4 \times 10^{-3}$	experiments (Robertson, 1959)
12,000	$(4.7 \pm 0.3) \times 10^{-3}$	present ODT

also determines the electric and ionic layers at the electrodes; and β expresses the strength of typical Coulomb forces in units of typical viscous forces. In a concentrated (dilute) ionic liquid (e.g. Lee et al., 2015), dielectric polarization is strong (weak) so that the dielectric permittivity is large (small). For constant electric charge on the ions, the Debye length has to increase (decrease) with β so that we do not consider β a variable control parameter. Instead, it is kept fixed at a typical value (e.g. Mani and Wang, 2020). In the following, only Re and Sc are varied. Preliminary results for voltage variations are discussed in Klein et al. (2022a) but omitted here. Further parameter variations are forthcoming and will be presented elsewhere.

4.2 Skin friction coefficient

Fig. 4 shows the turbulent drag enhancement in EHD Couette flow by the Sc and Re dependence of the skin friction coefficient C_f. The latter is evaluated based on the temporal-averaged model-resolved streamwise velocity profile, $\bar{u}(y) = \overline{u(y,t)}$, as

$$C_f = 2\frac{u_\tau^2}{U^2}, \tag{18}$$

where

$$u_\tau = \sqrt{\nu \left|\frac{\mathrm{d}\bar{u}}{\mathrm{d}y}\right|_w}. \tag{19}$$

ODT simulations conducted for $\hat{V} = 0$ under absence of EHD effects are used to determine the reference value $C_{f,0}$ that is used for normalization. Tab. 2 gives the reference values obtained with ODT in comparison to available reference experiments (Robertson, 1959) and DNS (Pirozzoli et al., 2014). The mean values are somewhat closer to experiments than DNS. The statistical significance of the present ODT results is within 2–5%, which is consistent with both reference data sets and considered sufficient for the present study. A similar level of agreement is observed for the EHD-enhanced case with Re = 3000 and Sc = 3 shown in Fig. 4, where ODT agrees with the available reference DNS by Ostilla-Mónico and Lee (2017). Both ODT and DNS exhibit weakly enhanced drag for the selected case set-up.

Present ODT results suggest that the turbulent drag is largely insensitive to EHD effects for low $\mathrm{Sc} \leqslant 10$ and low $\mathrm{Re} \leqslant 3000$ within the statistical significance of the model results. A significant increase of the turbulent drag is observed for $\mathrm{Sc} \geqslant 10$, exceeding 30% enhancement for $\mathrm{Sc} \geqslant 300$ at Re = 12,000. This has not previously been reported and cannot be reached with present DNS nor LES due to cost constraints and unknown parameterizations of the EHD effects, respectively.

The magnitude of the EHD-enhanced drag increases with Sc and Re, hinting at intense interactions of the turbulent flow with the electrokinetics as smaller flow scales develop. Interestingly, ODT predicts a change of the flow regime for the critical Schmidt number $\mathrm{Sc}_{\mathrm{crit}} \simeq 30$, which is obtained from the intersection of two empirical fitting functions that describe the nonsaturated drag

increase for the two Reynolds numbers investigated. The Re dependence of the fit coefficients suggests presence of multiscale feedback mechanisms in the boundary layer flow. The physical mechanism are not yet well understood, but based on the the model-resolved flow physics, we speculate that the ion concentrations and, hence, the electric field, have to sample details of the flow field. This is only possible when the concentration field exhibits smaller spatial scales the the velocity field. The Batchelor scale η_B (Batchelor, 1959) needs to be significantly smaller than the Kolmogorov scale η_K (Kolmogorov, 1941), or an otherwise representative viscous length scale of the boundary layer flow, so that $\eta_B/\eta_K = Sc^{-1/2} \ll 1$. Inserting $\mathrm{Sc}_{\mathrm{crit}} = 30$ yields $\eta_B/\eta_K \approx 0.18$, which is on the edge of the required inequality. The same argumentation holds for other Re and electrolytes, which have to fulfill the same criterion with respect to scale separation. This renders $\mathrm{Sc}_{\mathrm{crit}} \simeq 30$ a common point close to which parametric dependencies of $C_f/C_{f,0}$ on Sc should diverge when Re is increased. So, based on the constancy of $\mathrm{Sc}_{\mathrm{crit}}$ with respect to Re, it suffices to proves our point by fitting a two-parametric function for the nonsaturated skin friction drag increase across $\mathrm{Sc} \in [50, 500]$ for only two different Re. The functional form of the data in the semi-logarithmic plot suggest a logarithmic increase of C_f with Sc, which is confirmed by the fits in Fig. 4.

Note that the value $\mathrm{Sc}_{\mathrm{crit}} \simeq 30$ is consistent with the physics-based argumentation put forward by Ostilla-Mónico and Lee (2017). This suggests that the critical Schmidt number is manifestation of interacting dynamical processes on different spatio-temporal scales which is addressed by ODT. However, Ostilla-Mónico and Lee (2017) expect a mild drag reduction based on their low Re DNS when Sc is increased beyond $O(10)$, which is in strict contrast to the present ODT results. The fully coupled ODT results are consistent with the experimentally validated one-way coupled case discussed above which makes drag enhancement plausible also for the simulated fully coupled regime. Below, we investigate the turbulent boundary layer in order to shed more light on the physical mechanism behind the model prediction.

4.3 Viscous boundary layer

Fig. 5 shows law-of-the-wall plots for the dimensionless mean velocity deficit, $\bar{u}^+$, over the dimensionless boundary layer coordinate, y^+, given by

$$\bar{u}^+ = \frac{|\bar{u} - u_w|}{u_\tau}, \tag{20}$$

$$y^+ = \frac{y u_\tau}{\nu}. \tag{21}$$

ODT simulation results are shown for various Re, Sc, and $\hat{V}$ in order to assess which region of the boundary layer is influenced by EHD effects. The hydrodynamic law of the wall (e.g. (Pope, 2000)) is given for orientation and is given by the intersecting viscous sublayer, $\bar{u}^+(y^+) = y^+$ for $y^+ < 5$, and the turbulent log layer, $\bar{u}^+(y^+) = \kappa^{-1} \ln y^+ + B$ for $y^+ > 30$, where κ is the von Kármán constant and B the additive constant. We show the parameterization with $\kappa = 0.39$ and $B = 4.2$, which has been obtained by fitting experimental data for flat-plate boundary layers (Marusic et al., 2010).

In Fig. 5(a) ODT results for various Re are shown under absence of EHD effects ($\hat{V} = 0$). The results demonstrate that the present model formulation and calibration is capable of reproducing the law-of-the-wall exactly, except for some deficit in the buffer layer in between $y^+ \in [10, 100]$ when compared with reference DNS from Ostilla-Mónico and Lee (2017) for Re = 3000. The dimensionless viscous boundary layer profiles obtained with ODT collapse almost identically onto each other without outer layer effects. This demonstrates applicability of inner layer similarity for Couette flow.

ODT results for finite $\hat{V} = 10$ are shown in Fig. 5(b) for selected Re and Sc. EHD-induced turbulent drag enhancement manifests itself by an increase of u_τ due to constant U so that the maximum value, $\bar{u}^+(y^+ = h^+)$, is reduced. Compensating for the increase of the velocity gradient at the wall collapses the linear sublayer, but not the turbulent log layer. The latter is hence influenced by EHD effects that are associated with enhanced mixing which is consistent with the flattening of profile (increase of κ). Consistent with Fig. 4, marginal boundary layer modeifcations are observed for Sc = 3 for both Re, whereas a strong effect is seen for Sc = 300 at Re = 12,000. Latter case suggests that EHD effects result in a nonuniversal nonlinear modification of the log layer that is strongest towards the bulk. This suggests a modification of bulk turbulence by EHD effects which is further investigated below by analysis of the concentration boundary layers, electric potential, and detailed turbulence properties based on conditional statistics of the ODT eddy events.

4.4 Concentration boundary layer

In order to better understand the physical mechanism for EHD-enhanced drag in the fully coupled regime, we investigate below electric flow variables fields. We select $\hat{V} = 4$ to facilitate comparison with reference data. This change in the set-up only weakly reduces the magnitude of the drag enhancement (Klein and Schmidt, 2021; Klein et al., 2022a), but yields otherwise qualitatively similar results as in the case of $\hat{V} = 10$ studied above.

Fig. 6 shows the nontrivial equilibrium mean state that develops due to drift-diffusion effects, achieving a balance of the electric fluxes $F_\pm$, given in Eq. (17), subject to a zero-flux boundary condition. Within ODT, the total electric potential, $\Phi(y, t)$, varies in y and t. Following Ostilla-Mónico and Lee (2017), the total potential is separated into the perturbation potential, $\phi(y, t)$, and the background state, $\phi_0(y)$, which contains the boundary conditions and the corresponding solution to the 1-D Gauss law assuming absence of free electric charges ($c_\pm = 0$) in the bulk of the fluid. Switching off turbulence either by considering a quiescent flow state ($u_i = 0, U = 0$) or a laminar flow by selecting $\mathrm{Re} \lesssim O(100)$ or simply setting the ODT rate parameter to zero ($C = 0$) yields a stationary solution. This solution only depends on the electrolyte properties contained in the normalized Debye length λ_D/h and the supplied normalized voltage $\hat{V}$ (Ostilla-Mónico and Lee, 2017).

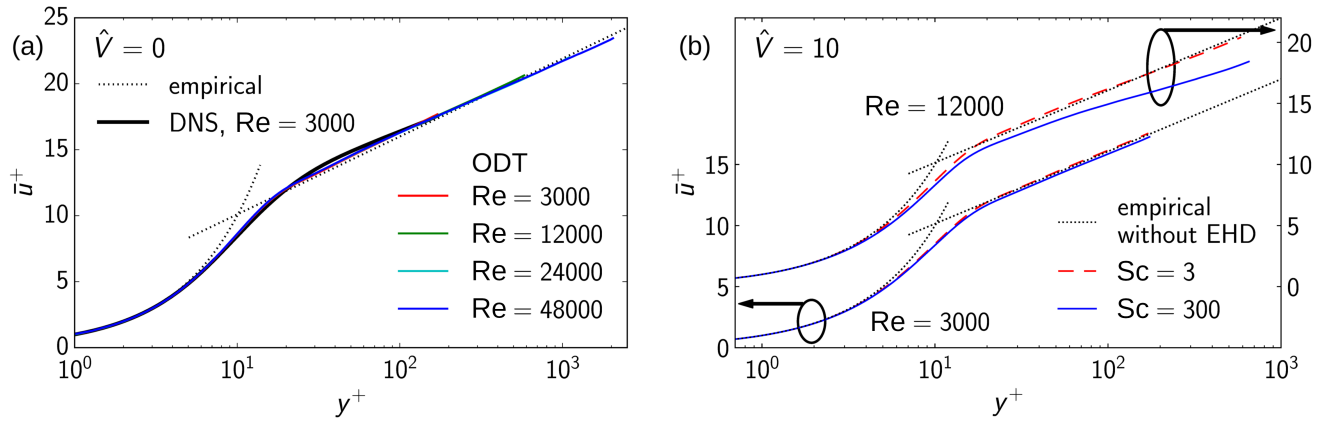

Fig. 5: Law-of-the-wall plots for the normalized mean velocity $\bar{u}^+(y^+)$. (a) Validation of the ODT momentum transfer without EHD effects. Reference DNS is from Ostilla-Mónico and Lee (2017). Mean velocity profiles collapse onto each other demonstrating boundary layer similarity. (b) Model prediction of velocity boundary layer modifications in the fully (fully) coupled EHD regime. The empirical log layer parameterization in all plots is from Marusic et al. (2010), which was obtained by measurements of high-Re flat-plate boundary layers.

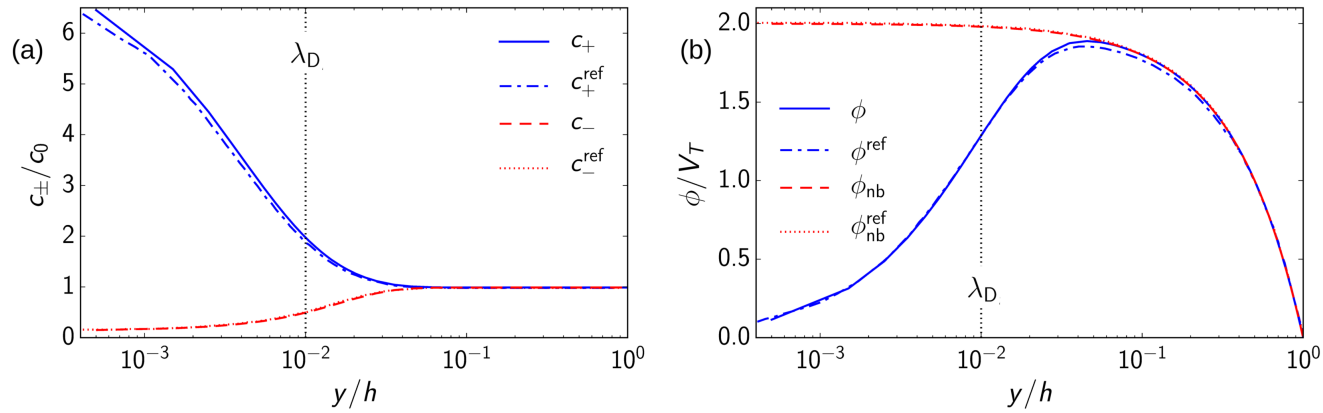

Fig. 6: (a) Concentration $c_\pm$ boundary layer applicable to quiescent and laminar flow conditions showing the equilibrium elektrokinetic state over the anode with space charge confined to the Debye layer of thickness λ_D. $\hat{V} = 4$ as in the reference DNS (superscript 'ref') of Ostilla-Mónico and Lee (2017). (b) Perturbation electric potential ϕ demonstrating the screening effect by assuming the field values for a entirely neutral bulk (subscript 'nb') outside the Debye layer.

The equilibrium ion concentrations $c_\pm(y)$ are localized in the Debye layer as shown in Fig. 6(a). The spatial structure of these fields gives rise to a wall-attached space-charge region (not shown) since the depletion of cations over the anode (anions over the cathode) and accumulation of anions at the anode (cations over the cathode) is asymmetric such that positive and negative charges no longer balance each other. The wall is responsible for the electric charge separation that relies on molecular drift-diffusion currents. The corresponding equilibrium perturbation electric field $\phi(y)$ is shown in Fig. 6(b). The spatial variation of ϕ demonstrates the screening effect of the wall-attached space-charge region. The perturbation electric field is zero at the wall but compensates the background field ϕ_0 in the bulk of fluid outside the Debye layer. This is visualized with the aid of the perturbation electric potential $\phi_{nb}(y) = -\phi_0(y)$, which refers to perfect screening of the wall boundary condition resulting in a perfectly neutral bulk.
Next, Fig. 7 shows temporal averaged ion concentrations $\bar{c}_\pm(y)$ obtained with fully coupled standalone ODT for turbulent EHD Couette flow under statistically stationary conditions. The mean concentrations are depleted due to turbulent mixing and entrainment of neutral bulk fluid so that the wall-attached space charge (not shown) is likewise reduced. The effect increases with Re due to increased mixing, but it also increases with Sc. For the latter, the physical mechanism is related to the charge separation mechanism, which is located at the wall, where it is governed by molecular drift-diffusion currents due to the zero-flux wall-boundary condition utilized for Eq. (17). A high Schmidt number implies low diffusivity and hence a low space-charge regeneration time due to limited mass transfer due to the competition with turbulent depletion explained above. To consolidate this hypothesis, the ion concentration flux is scaled by expressing it in units of the viscous momentum transfer to the wall. $F_\pm$ is divided by the reference concentration c_0 and u_τ. The former is the maximum possible depletion of cations over the anode (anions over the cathode) across the Debye boundary layer, which can be deduced from Fig. 6(b), whereas the latter is a measure for the viscous time scale expressed as a scale velocity. Factoring the channel half-height h, which is identical to the thickness of the turbulent boundary layer for fully developed flow, yields

$$\frac{F_\pm(c_\pm)}{c_0 u_\tau} = \frac{D}{u_\tau h}\left(-\frac{h}{c_0}\frac{\partial c_\pm}{\partial y} \mp \frac{D c_\pm h}{c_0 V_T}\frac{\partial \Phi}{\partial y}\right), \tag{22}$$

where the prefactor expresses the space-charge regeneration time scale in units of the viscous time scale for imbalanced nonzero

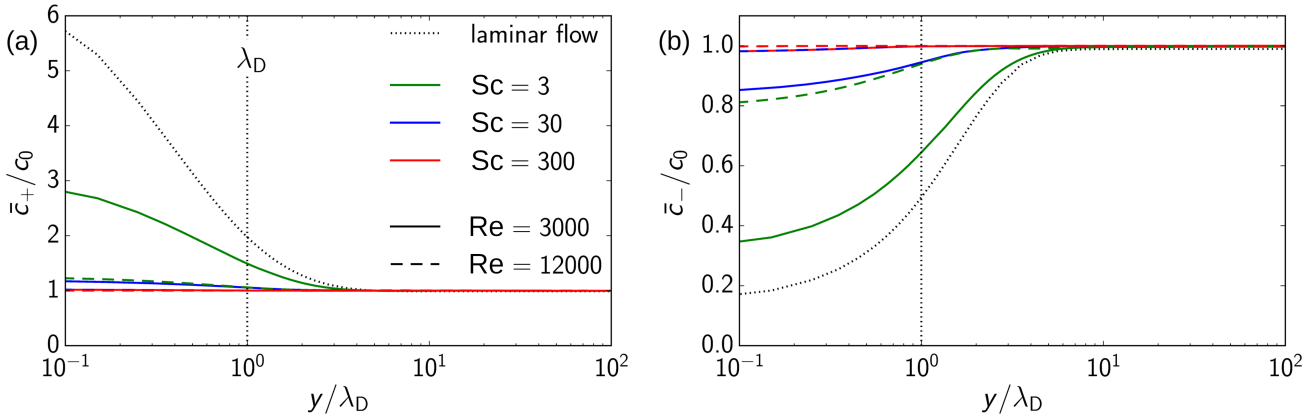

Fig. 7: ODT mean concentration boundary layer over the anode for turbulent flow conditions for various Re and Sc, but fixed $\hat{V} = 4$, $\beta = 0.5$, and $\lambda_D/h = 0.01$. (a) Anion concentration $\bar{c}_+$ and (b) cation concentration $\bar{c}_-$ exhibiting a weakening of the equilibrium state shown in Fig. 6(a) due to turbulent entrainment of neutrally charged bulk fluid. Mean deviations from c_0 remain confined to the Debye layer of thickness λ_D.

flux off the wall during the transient relaxation. The momentary momentum flux to the wall, $F_i = -\nu\,(\partial u_i/\partial y)$, is correspondingly expressed in viscous units as $F_i^+ = F_i/u_\tau^2 = -\mathrm{Re}_\tau^{-1}(\partial u_i^+/\partial y^+)$. The prefactor in Eq. (22) is dimensionless, representing the inverse friction Peclet number, $\mathrm{Pe}_\tau = D/(u_\tau h) = Sc^{-1}\mathrm{Re}_\tau^{-1}$. The dimensionless ion fluxes due to drift-diffusion processes are, hence, by a factor Sc^{-1} smaller than the dimensionless viscous momentum flux. This implies a reduced space-charge regeneration time for high Sc irrespective of Re_τ, since, by dimensional arguments, $\mathrm{Sc} = \nu/D = \tau_{\mathrm{diff}}/\tau_{\mathrm{visc}}$ is precisely the ratio of the molecular diffusion time scale, τ_{diff}, and the viscous time scale, τ_{visc}. This explains why, for strong enough turbulence, the near-wall space-charge regions are depleted, as captured by the ODT.

4.5 Features of emerging transients and scale interactions

A consequence of the reduction of the mean space charge in the Debye layers is a decrease of the screening effect. The perturbation electric potential ϕ reduces in the bulk, as shown previously for preliminary ODT results (Schmidt et al., 2021), yielding stronger total electric fields in the bulk. Small-scale features at the wall strongly affect the bulk electric field remote from the wall. This constitutes a multiscale and nonlocal feedback mechanism in wall-bounded fully-coupled EHD turbulence that is investigated next. Fig. 8 shows space-time diagrams of the ODT-resolved profile evolution of the momentary total electric potential $\Phi(y,t) = \phi(y,t) + \phi_0(y)$ normalized by half of the supplied voltage difference V for various Sc keeping all other parameters fixed at the values given in the caption of Fig. 4. The stochastically sampled sequence of ODT eddy events in a flow realization is shown on top of the continuous profile evolution by black line intervals. This demonstrates how turbulence scales are affected by and interact with the momentary electric field. Both the evolution of the model-resolved electric potential and the sequence of turbulent eddies are a result of the fully coupling by incorporating changes in the electrostatic potential energy, Eq. (11), in the eddy rate expression, Eq. (3). By varying Sc, the space-charge regeneration time scale is modified, resulting in transient screening effects. The screening governs the bulk electric field, leading to shorter or longer transients in the electric potential depending on Sc as shown in Fig. 8. Small Sc = 0.3 and even moderate Sc = 3 imply short equilibration time scales so that transients are too short to allow for a notable interaction of bulk turbulence with nonzero model-resolved electric fields, $E_2 = -\partial\Phi/\partial y$. The fast fluctuations in the electric potential average out not allowing for changes of the velocity due to inertia. Large Sc = 300, by contrast, yield very long transients and prevented screening so that bulk turbulence effectively experiences an almost homogeneous background electrical field. It is therefore not surprising that bulk turbulence is affected the most by EHD effects, resulting in visually smaller turbulence scales. Fig. 9 shows distribution functions of the stochastically sampled ODT eddy events for various Re and Sc corresponding to cases in Figs. 4 and 8. The cumulative density function (c.d.f.) for the eddy size l is shown in Fig. 9(a). By shifting towards smaller scales with increasing Sc at Re = 12,000, the c.d.f. demonstrates that small-scale turbulence intensified by EHD effects, but only when Re is sufficiently large (Klein and Schmidt, 2021). This is consistent with the observation for C_f in Fig. 4 and also in line with the physical interpretation of the viscous boundary layer $\bar{u}^+(y^+)$ shown in Fig. 5(b) together with the mean field effects shown in Figs. 7 and 8 above.

In order to further consolidate the physical interpretation, Fig. 9(b) shows the corresponding probability density function (p.d.f.) of the lower edge ODT eddy location y_0 showing only the bottom half $[0, h]$ of the flow domain. The p.d.f. reveals a change in the turbulent flow regime when Re is increased. While eddy locations are not affected by elektrokinetics for low Re = 3000, a significant reduction of wall-attached eddies (Townsend, 1976) is observed for moderate Re = 12,000. In addition, the eddy location p.d.f. switches from a unimodal distribution at Re = 3000, where the maximum is located at the wall, to a bimodal distribution at Re = 12,000. The developing broad peak on the right of the plotting range corresponds to EHD-enhanced bulk turbulence in the center of the flow domain. The eefect increases with Sc and is consistent with the qualitative observation in Fig. 8. This suggests that turbulent drag enhancement in fully coupled EHD Couette flow is the result of EHD-enhanced small-scale bulk turbulence. The increased mixing more efficiently depletes the near-wall space charge by entrainment of neutral bulk fluid. The EHD-enhanced mixing, therefore, sustains the reduced screening, yielding strong bulk electric fields. This constitutes a positive feedback mechanism involving processes on multiple scales, coupling wall properties and bulk flow.

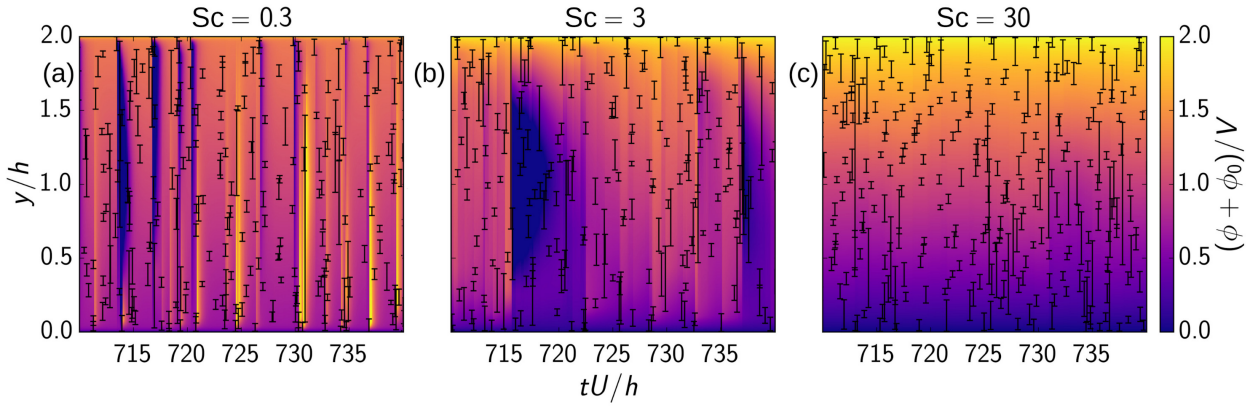

Fig. 8: Hovmöller diagrams of the the momentary total electric potential, $\Phi = \phi + \phi_0$, for various Sc using fixed Re = 12,000, $\beta = 0.5$, $\lambda_D/h = 0.01$, and $\hat{V} = 10$, showing the spatio-temporal evolution of , resolved along the ODT domain within the standalone model formulation. (a) Sc = 0.3. (b) Sc = 3. (c) Sc = 30. ODT eddy events are overlaid by black vertical line intervals showing their size, location, and time of occurrence.

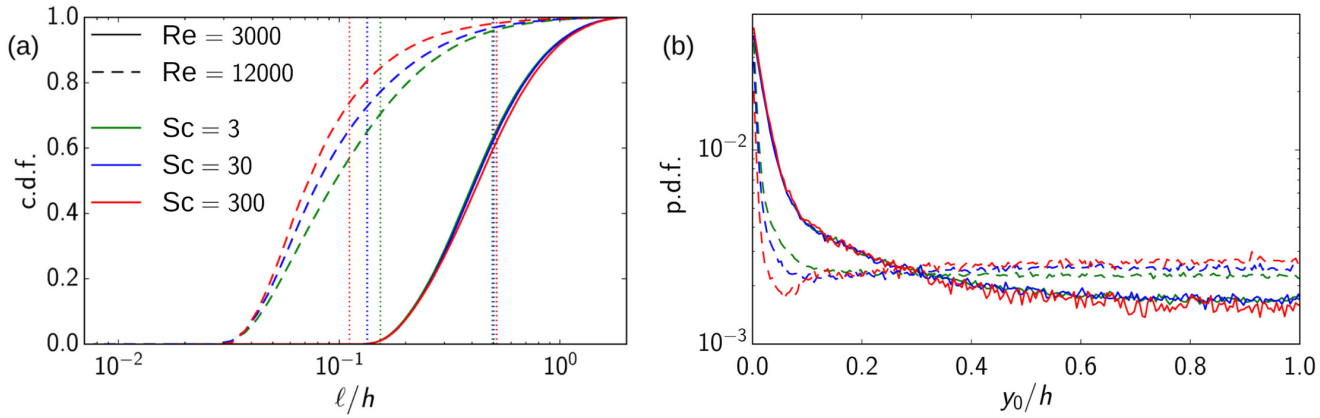

Fig. 9: ODT eddy event statistics for various Sc and Re using fixed $\beta = 0.5$, $\lambda_D = 0.01$, and $\hat{V} = 10$. (a) Cumulative density function (c.d.f.) of the eddy size l. Vertical dotted lines with matching color indicate the expectation value for l for various Sc and Re. This figure is reproduced from Klein and Schmidt (2021) under Creative Commons 4.0 (CC-BY-NC) License. (b) Probability density function (p.d.f.) of the lower-edge eddy location y_0. Wiggles are due to finite sample variability.

4.6 Discussion

The dimensionally reduced, fully coupled ODT formulation for electroconvection has been utilized to investigate EHD-induced enhancement of the turbulent drag by broadly varying the molecular Schmidt number for sufficiently large turbulence intensities. Within the 1-D framework, the model results suggest a multiscale feedback mechanism between EHD-enhanced bulk turbulence and increased entrainment of bulk fluid into the boundary layer that reduces screening effects giving rise tstronger electric fields in the bulk. This mechanism is self-sustaining and efficient for high Schmidt numbers slowing down molecular drift-diffusion currents that result in long charge-relaxation time scales and long transients, increasing the coupling efficiency of hydrodynamic and electrokinetic processes.

A limitation of the present standalone model is the 1-D formulation of the Gauss law. The 3-D spatial structure of the electric potential is not resolved and it is implied that ions and electric fields are organized in large scale structures forming layers that are parallel to the wall. This might not be physically justified under all circumstances. The result would be an overestimation of turbulence effects, which means an overestimation of the magnitude of the drag enhancement, but less of the sign. This is because, in the 1-D representation, both the strength of bulk electric fields (due to differences in the spatial structure between the operator Green's function for the 3-D and 1-D Gauss law, e.g. Jackson, 1975) and the entrainment (due to map-based advection) would be overestimated together, resulting in artificial drag enhancement. Since DNS are to costly to reach high enough Reynolds and Schmidt numbers, and the modeling required for LES is unknown, it would be interesting to assess the present model prediction by dedicated laboratory experiments.

5 Conclusion

EHD turbulence denotes a chaotic flow that is influenced by inertial, viscous, and Coulomb forces across a range of scales. Dynamical processes are nonuniversal and reach down to the diffusive scales while coupling to the large scales due to the nonlocal interaction of Coulomb forces, which result from the interaction of local electric charges with the background electric fields. This places a strong burden on numerical simulation and modeling of EHD flows. Not only because of multiphysical flow

features but also because the emerging EHD scales can be even smaller than the Kolmogorov and Batchelor scales, increasing the cost of numerical simulations. In applications, like membraneless redox flow batteries, liquid metal batteries, electrochemistry applications, and electrostatic precipitators, EHD flows are confined so that velocity and scalar boundary layers and the surface physics at domain walls or internal interfaces have to be resolved. Resolution and forward-modeling requirements have been addressed here by utilizing the stochastic one-dimensional turbulence (ODT) model for numerical investigation of wall-bounded EHD-enhanced flows.

In one-way coupled vertical EHD pipe flow with a coaxial central electrode, ODT captures some relevant drag enhancement effects, relating them to increased mixing. Turbulent drag is enhanced by an EHD-based amplification of the rate of change of the turbulent kinetic energy as revealed by an analysis of the contributions to the pressure drop per unit pipe length of the spatially developing flow. Based on boundary layer similarity regime overlap, we assert that the mechanism is at work for the radial direction in the gas-phase EHD pipe flow must be similar to that in temporally evolving EHD Couette flow of an ionic liquid that facilitates a more detailed investigation of the boundary layer flow.

In fully (fully) coupled EHD Couette flow, ODT predicts EHD-enhanced bulk turbulence that affects the entire turbulent boundary layer, giving rise to a multiscale coupling of wall and bulk properties. The turbulent drag increases like $C_f \sim \ln(\mathrm{Sc})$ for $\mathrm{Sc}_{crit} \approx 30 < \mathrm{Sc} < 500$ for the nonsaturated drag enhanced regime for all turbulent cases investigated. The results suggest that charge carriers have to be immobile enough to allow for long transients and slow charge relaxation in order to allow for strong coupling of hydrodynamic entrainment of neutral bulk fluid into the electric boundary layer and electrokinetic charge separation by molecular drift-diffusion currents. Albeit the physical mechanism is consistently represented in the model, the magnitude of the drag enhancement may be overestimated. Some model predictions therefore await experimental validation.

We conclude that ODT is a self-contained, dimensionally reduced flow model that combines fidelity, predictability, and numerical efficiency. We have demonstrated the applicability to EHD-enhanced flows, which facilitates future application as advanced subgird-scale model in LES for advanced modeling of EHD turbulence.

Acknowledgements

We thank Rodolfo Ostilla-Mónico for fruitful discussion and making reference direct numerical simulation data for EHD Couette flow available. We likewise thank Ulrich Riebel and Christian Bacher for discussion and insight into EHD pipe flow experiments. We furthermore express our gratitude to David O. Lignell for discussion and making a basic version of the mesh-adaptive ODT code publicly available at URL https://github.com/BYUignite/ODT (last accessed 2022-10-17).

This research is supported by the European Regional Development Fund (Grant number StaF 23035000), the German Federal Government, the Federal Ministry of Education and Research and the State of Brandenburg within the framework of the joint project EIZ: Energy Innovation Center (project numbers 85056897 and 03SF0693A) with funds from the Structural Development Act (Strukturstärkungsgesetz) for coal-mining regions. M.K. furthermore acknowledges support by the BTU Graduate Research School (Conference Travel Grant).

References

J. P. Abraham, E. M. Sparrow, and J. C. K. Tong. Breakdown of laminar pipe flow into transitional intermittency and subsequent attainment of fully developed intermittent or turbulent flow. *Numer. Heat Transfer, Part B*, 54(2):103–115, 2008. doi: 10.1080/10407790802156178.

W. T. Ashurst and A. R. Kerstein. One-dimensional turbulence: variable-density formulation and application to mixing layers. *Phys. Fluids*, 17(2):025107, 2005. doi: 10.1063/1.1847413.

C. Bacher and U. Riebel. Electrohydrodynamically enhanced mass transfer in a wetted-wall column. *Chem. Eng. Res. Des.*, 167: 183–197, 2021. doi: 10.1016/j.cherd.2021.01.006.

C. Bacher, V. Lebedynskyy, S. Fischer, and U. Riebel. Discharge electrode geometry and energy efficiency in a one-stage wire–tube electrostatic precipitator operating at high concentrations of submicron liquid aerosol. *Environ. Technol.*, 41(16):2096–2108, 2020. doi: 10.1080/09593330.2018.1555613.

G. K. Batchelor. Small-scale variation of convected quantities like temperature in turbulent fluid. Part 1. General discussion and the case of small conductivity. *J. Fluid Mech.*, 5:113–133, 1959.

J. H. Davidson and E. J. Shaughnessy. Turbulence generation by electric body forces. *Exp. Fluids*, 4(1):17–26, 1986. doi: 10.1007/BF00316781.

K. Duraisamy, G. Iaccarino, and H. Xiao. Turbulence modeling in the age of data. *Annu. Rev. Fluid Mech.*, 51(1):357–377, 2019. doi: 10.1146/annurev-fluid-010518-040547.

M. M. Fragner and H. Schmidt. Investigating asymptotic suction boundary layers using a one-dimensional stochastic turbulence model. *J. Turbul.*, 18(10):899–928, 2017. doi: 10.1080/14685248.2017.1335869.

E. D. Gonzalez-Juez, A. R. Kerstein, and D. O. Lignell. Reactive Rayleigh-–Taylor turbulent mixing: a one-dimensional-turbulence study. *Geophys. Astro. Fluid Dyn.*, 107(5):506–525, 2013. doi: 10.1080/03091929.2012.736504.

J. D. Jackson. *Classical Electrodynamics*. Wiley, New York, NY, 2nd edition, 1975. ISBN 978-0471431329.

Y. Ju and W. Sun. Plasma assisted combustion: dynamics and chemistry. *Prog. Energy Combust. Sci.*, 48:21–83, 2015. doi: https://doi.org/10.1016/j.pecs.2014.12.002.

A. R. Kerstein. One-dimensional turbulence: Model formulation and application to homogeneous turbulence, shear flows, and buoyant stratified flows. *J. Fluid Mech.*, 392:277–334, aug 1999. doi: 10.1017/S0022112099005376.

A. R. Kerstein. Reduced numerical modeling of turbulent flow with fully resolved time advancement. Part 1. Theory and physical interpretation. *Fluids*, 7(2):76, 2022. doi: 10.3390/fluids7020076.

A. R. Kerstein, W. T. Ashurst, S. Wunsch, and V. Nilsen. One-dimensional turbulence: vector formulation and application to free-shear flows. *J. Fluid Mech.*, 447:85–109, May 2001. doi: 10.1017/S0022112001005778.

G. K. El Khoury, P. Schlatter, A. Noorani, P. F. Fischer, G. Brethouwer, and A. V. Johansson. Direct numerical simulation of turbulent pipe flow at moderately high Reynolds numbers. *Flow, Turbul. Combust.*, 91(3):475–495, Oct 2013. doi: 10.1007/s10494-013-9482-8.

M. Klein and H. Schmidt. Towards a stochastic model for electrohydrodynamic turbulence with application to electrolytes. *Proc. Appl. Math. Mech.*, 20:e202000128, 2020. doi: 10.1002/pamm.202000128.

M. Klein and H. Schmidt. Investigating Schmidt number effects in turbulent electroconvection using one-dimensional turbulence. *Proc. Appl. Math. Mech.*, 21:e202100147, 2021. doi: 10.1002/pamm.202100147.

M. Klein, C. Zenker, and H. Schmidt. Small-scale resolving simulations of the turbulent mixing in confined planar jets using one-dimensional turbulence. *Chem. Eng. Sci.*, 204:186–202, 2019. doi: 10.1016/j.ces.2019.04.024.

M. Klein, J. A. Medina Méndez, and H. Schmidt. Modeling electrohydrodynamically enhanced drag in channel and pipe flows using one-dimensional turbulence. In J. Vad, editor, *Proc. Conference on Modelling Fluid Flow (CMFF'22)*, pages 82–91. University of Technology and Economics, Department of Fluid Mechanics, Budapest, Hungary, 2022a. ISBN 978-9634218814. URL https://www.cmff.hu/pdf/CMFF22_Conference_Proceedings.pdf. Last accessed 2022-10-28. Contribution ID CMFF22-015.

M. Klein, H. Schmidt, and D. O. Lignell. Stochastic modeling of surface scalar-flux fluctuations in turbulent channel flow using one-dimensional turbulence. *Int. J. Heat Fluid Flow*, 93:108889, 2022b. doi: 10.1016/j.ijheatfluidflow.2021.108889.

A. N. Kolmogorov. The local structure of turbulence in incompressible viscous fluid for very large Reynolds numbers. *Dok. Akademii Nauk SSSR*, 30:299–303, 1941.

S. Laohalertdecha, P. Naphon, and S. Wongwises. A review of electrohydrodynamic enhancement of heat transfer. *Renewable Sustainable Energy Rev.*, 11(5):858–876, 2007. doi: 10.1016/j.rser.2005.07.002.

A. A. Lee, D. Vella, S. Perkin, and A. Goriely. Are room-temperature ionic liquids dilute electrolytes? *J. Phys. Chem. Lett.*, 6(1): 159–163, 2015. doi: 10.1021/jz502250z. PMID: 26263105.

K. Lee, V. Venugopal, and S. S. Girimaji. Pressure-strain energy redistribution in compressible turbulence: return-to-isotropy versus kinetic-potential energy equipartition. *Phys. Scr.*, 91(8):084006, 2016. doi: 10.1088/0031-8949/91/8/084006.

D. Lignell, V. B. Lansinger, J. A. Medina Méndez, M. Klein, A. R. Kerstein, H. Schmidt, M. Fistler, and M. Oevermann. One-dimensional turbulence modeling for cylindrical and spherical flows: model formulation and application. *Theor. Comput. Fluid Dyn.*, 32(4):495–520, Aug 2018. doi: 10.1007/s00162-018-0465-1.

D. O. Lignell, A. R. Kerstein, G. Sun, and E. I. Monson. Mesh adaption for efficient multiscale implementation of one-dimensional turbulence. *Theor. Comp. Fluid Dyn.*, 27(3):273–295, 2013. doi: 10.1007/s00162-012-0267-9.

A. Mani and K. M. Wang. Electroconvection near electrochemical interfaces: experiments, modeling, and computation. *Annu. Rev. Fluid Mech.*, 52(1):509–529, 2020. doi: 10.1146/annurev-fluid-010719-060358.

I. Marusic, B. J. McKeon, P. A. Monkewitz, H. M. Nagib, A. J. Smits, and K. R. Sreenivasan. Wall-bounded turbulent flows at high Reynolds numbers: recent advances and key issues. *Phys. Fluids*, 22:065103, 2010. doi: 10.1063/1.3453711.

J. A. Medina Méndez. *Application of the One-Dimensional Turbulence model to electrohydrodynamically enhanced internally forced convective flows*. PhD thesis, Brandenburgische Technische Universität Cottbus-Senftenberg, Cottbus, Germany, 2020.

J. A. Medina Méndez, M. Klein, and H. Schmidt. One-dimensional turbulence investigation of variable density effects due to heat transfer in a low Mach number internal air flow. *Int. J. Heat Fluid Flow*, 80:108481, 2019. doi: 10.1016/j.ijheatfluidflow.2019.108481.

J. A. Medina Méndez, H. Schmidt, and U. Riebel. Towards a one-dimensional turbulence approach for electrohydrodynamic flows. In *11th Int. Symp. Turbul. Shear Flow Phen. (TSFP11)*, pages 1–6, Southampton, UK, 2019. ID 265.

J. A. Medina Méndez, C. Bacher, U. Riebel, and H. Schmidt. Electrohydrodynamically-enhanced drag in a vertical pipe-flow with a concentric electrode: a one-dimensional turbulence study. *Eur. J. Mech. – B/Fluids*, 95:240–251, 2022. ISSN 0997-7546. doi: 10.1016/j.euromechflu.2022.05.008.

J. R. Melcher. *Continuum Electromechanics*. MIT Press, Cambridge, MA, 1981. ISBN 978-0262131650.

D. A. Nelson, M. M. Ohadi, S. Zia, and R. L. Whipple. Electrostatic effects on pressure drop in tube flows. *Int. J. Heat Fluid Flow*, 11(4):298–302, 1990. doi: https://doi.org/10.1016/0142-727X(90)90053-E.

R. Ostilla-Mónico and A. A. Lee. Controlling turbulent drag across electrolytes using electric fields. *Faraday Discuss.*, 199: 159–173, 2017. doi: 10.1039/C6FD00247A.

S. Pandey, X. Chu, B. Weigand, E. Laurien, and J. Schumacher. Relaminarized and recovered turbulence under nonuniform body forces. *Phys. Rev. Fluids*, 5:104604, Oct 2020. doi: 10.1103/PhysRevFluids.5.104604.

A. Papoulis and S. U. Pillai. *Probability, Random Variables, and Stochastic Processes*. McGraw-Hill, New York, 4th edition, 2002.

S. Pirozzoli, M. Bernardini, and P. Orlandi. Turbulence statistics in Couette flow at high Reynolds number. *J. Fluid Mech.*, 758: 327–343, 2014. doi: 10.1017/jfm.2014.529.

S. B. Pope. *Turbulent Flows*. Cambridge University Press, 2000. ISBN 978-0521598866.

Rakhi, M. Klein, J. A. Medina Méndez, and H. Schmidt. One-dimensional turbulence modelling of incompressible temporally developing turbulent boundary layers with comparison to DNS. *J. Turbul.*, 20(8):506–543, 2019. doi: 10.1080/14685248.2019.1674859.

J. M. Robertson. On turbulent plane Couette flow. In *Sixth Midwestern Conference on Fluid Mechanics*, pages 169–182, University of Texas, Austin, 1959.

M. Robinson. Turbulent gas flow and electrostatic precipitation. *J. Air Pollut. Control Assoc.*, 18(4):235–239, 1968. doi: https://doi.org/10.1080/00022470.1968.10469120.

H. Schmidt, J. A. Medina Méndez, and M. Klein. EHD turbulence in channel flows with inhomogeneous electrical fields: a one-dimensional turbulence study. In *WCCM-ECCOMAS 2020*, pages 1–12. SCIPEDIA, 2021. doi: 10.23967/wccm-eccomas.2020.131.

S. Shiva Kumar and V. Himabindu. Hydrogen production by PEM water electrolysis — a review. *Mater. Sci. Energy Technol.*, 2 (3):442–454, 2019. doi: 10.1016/j.mset.2019.03.002.

B. D. Storey. Direct numerical simulation of electrohydrodynamic flow instabilities in microchannels. *Phys. D: Nonlin. Phen.*, 211 (1):151–167, 2005. doi: 10.1016/j.physd.2005.08.010.

A. A. R. Townsend. *The Structure of Turbulent Shear Flow*. Cambridge University Press, 2nd edition, 1976. ISBN 978-0521298193.

S. Wunsch and A. R. Kerstein. A stochastic model for high-Rayleigh-number convection. *J. Fluid Mech.*, 528:173–205, 2005. doi: 10.1017/S0022112004003258.

W. Zhao and G. Wang. Scaling of velocity and scalar structure functions in AC electrokinetic turbulence. *Phys. Rev. E*, 95(2): 023111, 2017. doi: 10.1103/PhysRevE.95.023111.

W. Zhao and G. Wang. Cascade of turbulent energy and scalar variance in DC electrokinetic turbulence. *Physica D: Nonlin. Phen.*, 399:42–50, 2019. doi: 10.1016/j.physd.2019.04.003.

W. Zhao and G. Wang. A tentative study of the transport of energy and other scalar quantities in forced turbulence driven by $\nabla^n a$-type volume forces. *J. Hydrodyn.*, 33(6):1271–1281, 2021. doi: 10.1007/s42241-022-0109-1.